RSC Advances

ROYAL SOCIETY OF CHEMISTRY

PAPER

View Article Online
View Journal | View Issue

Cite this: *RSC Adv.*, 2026, **16**, 953

Polyvinyl alcohol and hydroquinone-based electrolyte coupled with mesoporous carbon nitride for high energy density supercapacitors

Mustapha Balarabe Idris,* Bhekie B. Mamba and Fuku Xolile

The pursuit of next-generation supercapacitors with high energy density requires not only the design of robust electrode material, but also the engineering of the electrolyte. Herein, we explore a redox-mediated gel polymer electrolyte (GPE) using polyvinyl alcohol (PVA) and hydroquinone (HQ)/benzoquinone (BQ) couple to enhance the supercapacitive performance of mesoporous graphitic carbon nitride (mg-CN). The mg-CN nanosheet was synthesised *via* a carboxymethyl cellulose-assisted templating approach. The structural, spectroscopic and textural properties studies revealed the formation of mg-CN with abundant defect sites and sp^2 carbon domains as well as a hierarchical porous structure with a surface area of 139 m^2 g^{-1}. Owing to the reversible redox reaction of the HQ/BQ couple leading to pseudocapacitance, mg-CN delivered a specific capacitance of 481 F g^{-1} at a scan rate of 5 mV s^{-1} in the 1 M H_2SO_4 + 0.01 HQ-based electrolyte, which is more than twice that of pristine H_2SO_4 (198 F g^{-1}). Evidently, the capacitive-diffusive current contribution study indicated that 42.71% of the specific capacitance obtained in the HQ-based electrolyte is contributed by a diffusion-controlled process, as compared to the 19.81% obtained in the 1 M H_2SO_4 electrolyte. A symmetrical supercapacitor device fabricated using the redox-mediated GPE (1 M H_2SO_4 + PVA + 0.01 M HQ, PVA/HQ) exhibited a remarkable energy density of 47.42 Wh kg^{-1} at a power density of 6500 W kg^{-1}, along with superior cycling stability. Owing to the improvement in the ionic conductivity of the gel offered by the charge carriers originating from the HQ (1 M H_2SO_4 + PVA: 371.44 *vs.* PVA/HQ: 401.81 mS cm^{-1}), the device delivers an energy density of 47.42 Wh kg^{-1} when the power density is increased to 6500 W kg^{-1}, an indication that the PVA/HQ electrolyte can be employed for the fabrication of a high-rate supercapacitor.

Received 30th October 2025
Accepted 22nd December 2025

DOI: 10.1039/d5ra08363j

rsc.li/rsc-advances

1 Introduction

The global shift towards renewable energy sources has intensified the quest for the development of advanced electrochemical energy storage systems.[1,2] Among them, supercapacitors are gaining attention due to their superb power density, extended cycle life, and rapid charge–discharge capability.[3] One major drawback of supercapacitors is low energy density, which limits their application in renewable energy storage systems where high energy density is very crucial. Over the years, various strategies have been adopted to improve their energy density, approaching that of rechargeable batteries.[4–8] Among the key components that dictate the performance of supercapacitors, the electrolyte plays a crucial role in governing ion transport, interfacial charge storage, and overall energy efficiency.[9] Although aqueous electrolytes exhibit superior ionic conductivity and are considered eco-friendly, limited voltage windows and the possibility of leakage have restricted their full utilisation for the fabrication of high-energy-density supercapacitors.[10] In recent years, gel polymer electrolytes (GPEs) have emerged as a promising alternative, combining the mechanical robustness of polymers with the ionic conductivity of liquid electrolytes.[11,12] Further enhancement of GPEs *via* redox-active mediators introduces an additional faradaic charge storage mechanism, enabling synergistic pseudocapacitance alongside electric double-layer capacitance.[11,13,14] This strategy not only elevates the specific capacitance but also broadens the operational voltage window and improves energy density, making redox-mediated GPEs a compelling choice for next-generation supercapacitors.

Graphitic carbon nitride (g-CN) is a semi-conductive material possessing high nitrogen content, excellent mechanical flexibility and environmental friendliness. Due to these appealing properties, g-CN has garnered significant attention for various applications, including sensing, photocatalysis, and remediation of environmental pollutants, among others. However, its relatively low surface area and limited electrical conductivity have limited its utilisation as an electrode material for SCs. This has necessitated the formation of composites of g-CN with various materials, enhancing its overall capacitance performance. For

---

Institute for Nanotechnology and Water Sustainability, College of Science, Engineering and Technology, University of South Africa, Florida Science Campus, 1710, South Africa. E-mail: idrisbm@unisa.ac.za

instance, nanostructured needle-like $NiCo_2O_4$ on g-CN exhibited a capacitance of 253 F g^{-1} at a current density of 2 A g^{-1} in 6 M KOH.[15] Nickel cobalt sulfide nanosheets grown on porous g-CN nanosheets delivered a very high capacitance of 506 F g^{-1} at a current density of 1 A g^{-1} in 2 M NaOH. It is worth mentioning that the majority of the obtained high capacitance is attributed to the pseudo-capacitance behaviour of $NiCo_2S_4$.[16] Zhang *et al.*[17] reported a specific capacitance of 167 F g^{-1} at a current density of 1 A g^{-1} in Li_2SO_4 electrolyte for graphite-like g-CN hybridised α-Fe_2O_3 hollow microspheres synthesised by ionic liquid-assisted solvothermal method. A composite of reduced graphene oxide and g-CN nanosheet delivered a specific capacitance of 288 F g^{-1} at a current density of 0.5 A g^{-1} in 6 M KOH.[18] Besides composite formation, the introduction of mesoporosity into their structural frameworks and the modification of the surface functional group of g-CN have been reported as a facile approach to improve its supercapacitive properties.[19–22] For instance, a facile soft template method was adopted to introduce mesoporosity into pristine g-CN and the material, termed as mesoporous graphitic carbon nitride (mg-CN), delivered a specific capacitance of 244 F g^{-1} at a current density of 0.5 A g^{-1} in 1 M H_2SO_4.[23] A mg-CN synthesised through the hard template method exhibited a specific capacitance of 322 F g^{-1} at a current density of 0.5 A g^{-1}. Although numerous studies have examined the supercapacitive performance of various carbon-based materials in redox additive gel polymer electrolytes,[24] the energy density remains limited. Herein, we explore a redox-mediated GPE using PVA and HQ/BQ couple to enhance the supercapacitive performance of mg-CN. The novelty of the present work lies in integrating an mg-CN electrode with hierarchical mesoporosity and sp^2 carbon domains into a PVA/HQ/BQ-based GPE. This combination simultaneously (i) increases the accessible pseudocapacitive sites through redox shuttling, (ii) improves ionic transport by modestly increasing gel ionic conductivity, and (iii) preserves gel mechanical integrity by using a low HQ concentration. A symmetrical supercapacitor device fabricated using the redox-mediated GPE PVA/HQ exhibited a remarkable energy density of 47.42 Wh kg^{-1} at a power density of 6500 W kg^{-1}, along with superior cycling stability.

2 Materials and methods

All precursors utilised in the present study were either purchased from Aldrich or Alfa Aesar and used as-received.

2.1 Synthesis of mg-CN

In a typical synthesis, 250 mg of sodium carboxymethylcellulose was added to 10 mL of ethanol under stirring. Subsequently, 20 mL of double-distilled water was added while maintaining the constant. To the above thick milky solution, 2 g of hexamethylenetetramine was added, and the temperature of the reaction mixture was raised to 80 °C and further stirred for 30 minutes. The obtained gel was then transferred into a Petri dish and dried at 80 °C in a hot air oven overnight. The obtained dried gel was ground using a mortar and pestle, transferred to a crucible, and then carbonised at 600 °C for 4 hours in static air. Finally, the sample was washed with 1 M HCl and dried in air at 80 °C for 12 hours.

2.2 Synthesis of HQ–PVA GPE

In a typical synthesis, 1 g of PVA with an average molecular weight of 146 000–186,000 was added to 10 mL of deionised water under vigorous conditions at 95 °C for 2 h. To this mixture, 10 mL of 1 M H_2SO_4 and 0.16624 g of benzoquinone (equivalent to 0.01 M) were added, and stirring was maintained for another 1 hour. The obtained gel was transferred into a Petri dish and frozen at −16 °C for 12 hours, then thawed at room temperature for 12 hours and labelled as 1 M H_2SO_4 + PVA + 0.01 M HQ. For comparison, a PVA GPE was prepared under the same conditions but without the addition of benzoquinone, and is denoted as 1 M H_2SO_4 + PVA.

2.3 Physicochemical characterization of as-prepared mg-CN

The degree of crystallinity and graphitisation in the as-prepared sample was assessed using a Rigaku MiniFlex 300/600 diffractometer equipped with Cu Kα ($\lambda = 1.5406$ Å) and a B&W TEK i Raman Plus spectrometer using a green laser (wavelength = 532 nm), respectively. The surface and bulk chemical composition of the as-prepared sample was evaluated using Thermo Scientific K-Alpha X-ray photoelectron spectroscopy and PerkinElmer Spectrum One Fourier transform infra-red spectroscopy, respectively. The FEI Tennai F30-S TWIN high-resolution transmission electron microscope (HR-TEM) and ZEISS field-emission scanning electron microscope (FE-SEM) were utilised to study the microstructures of the sample. The textural properties of the sample, including surface area, pore volume and pore size distribution, were evaluated using Quantachrome surface area analyser. The sorption study was conducted after the as-prepared sample was degassed at 150 °C for 4 hours under vacuum.

2.4 Characterization of 1 M H_2SO_4 + PVA + 0.01 M HQ and 1 M H_2SO_4 + PVA

The thermal stability of both 1 M H_2SO_4 + PVA + 0.01 M HQ and 1 M H_2SO_4 + PVA was conducted using DSC 3+/700METTLER differential scanning calorimetry (DSC). The ionic conductivity of the 1 M H_2SO_4 + PVA + 0.01 M HQ and 1 M H_2SO_4 + PVA was measured using electrochemical impedance spectroscopy (EIS) in the frequency range of 0.01 to 104 Hz. The gel electrolytes were sandwiched between stainless steel foil. Subsequently, the ionic conductivity (σ_c, mS cm^{-1}) was calculated using;

$$\sigma_c = \frac{s}{RA} \tag{1}$$

where s is the thickness of the sample (cm), R is the bulk ionic resistance (Ω) obtained from EIS, and A is the area of the gel electrolyte (cm^2).

2.5 Electrochemical studies in a three-electrode configuration

The capacitance properties of the as-prepared sample were evaluated using mg-CN on coated stainless steel (SS) foil as a working electrode, Ag/AgCl as a reference electrode and Pt foil as a counter electrode in both pristine electrolyte (1 M H_2SO_4) and redox-additive based electrolyte (1 M H_2SO_4 + 0.01 M HQ). The working electrode was fabricated by casting a homogeneous slurry consisting of 80% mg-CN, 10% conductive carbon additive (Super P, carbon black), and 10% binder (poly(vinylidene fluoride)) on both sides of the foil and then dried at 90 °C overnight. Capacitance studies were conducted by running cyclic voltammograms (CVs) at various scan rates.

2.6 Fabrication of symmetrical supercapacitor devices using redox-mediated additive electrolyte and its capacitance studies

The slurry of mg-CN was utilised to coat one side of battery-grade SS foil, and the other side was wrapped with a Teflon tape. The mass loading of the material in each electrode is maintained at 2 mg. Subsequently, the two electrodes were sandwiched between either 1 M H_2SO_4 + PVA + 0.01 M HQ or 1 M H_2SO_4 + PVA electrolyte. The capacitance performances of devices fabricated with either 1 M H_2SO_4 + PVA + 0.01 M HQ or 1 M H_2SO_4 + PVA PVA–H_2SO_4 electrolyte were evaluated by recording CVs and galvanostatic charge–discharge cycles at different current densities. The specific capacitances, energy and power density of devices were calculated using;

$$\text{Specific capacitance(SC)} = \frac{I \times \Delta t}{\Delta V \times m} \tag{2}$$

$$\text{Energy density}(E) = \frac{1}{2}\text{CV}^2 \times \frac{1000}{3600} \tag{3}$$

$$\text{Power density}(P) = \frac{E \times 3600}{\Delta t} \tag{4}$$

where SC is specific capacitance (F g^{-1}), V is the working potential of the device (V), m is the mass of the electrode material, and t is the discharging time (s).[25,26]

3 Results and discussion

3.1 Physicochemical characterisation of as-prepared mg-CN

The powered X-ray diffraction pattern presented in Fig. 1a exhibits two broad diffraction peaks at approximately 24.48° (002) and 43.01° (101), corresponding to the graphite-like stacked structures in g-CN and amorphous carbon.[18,21] The

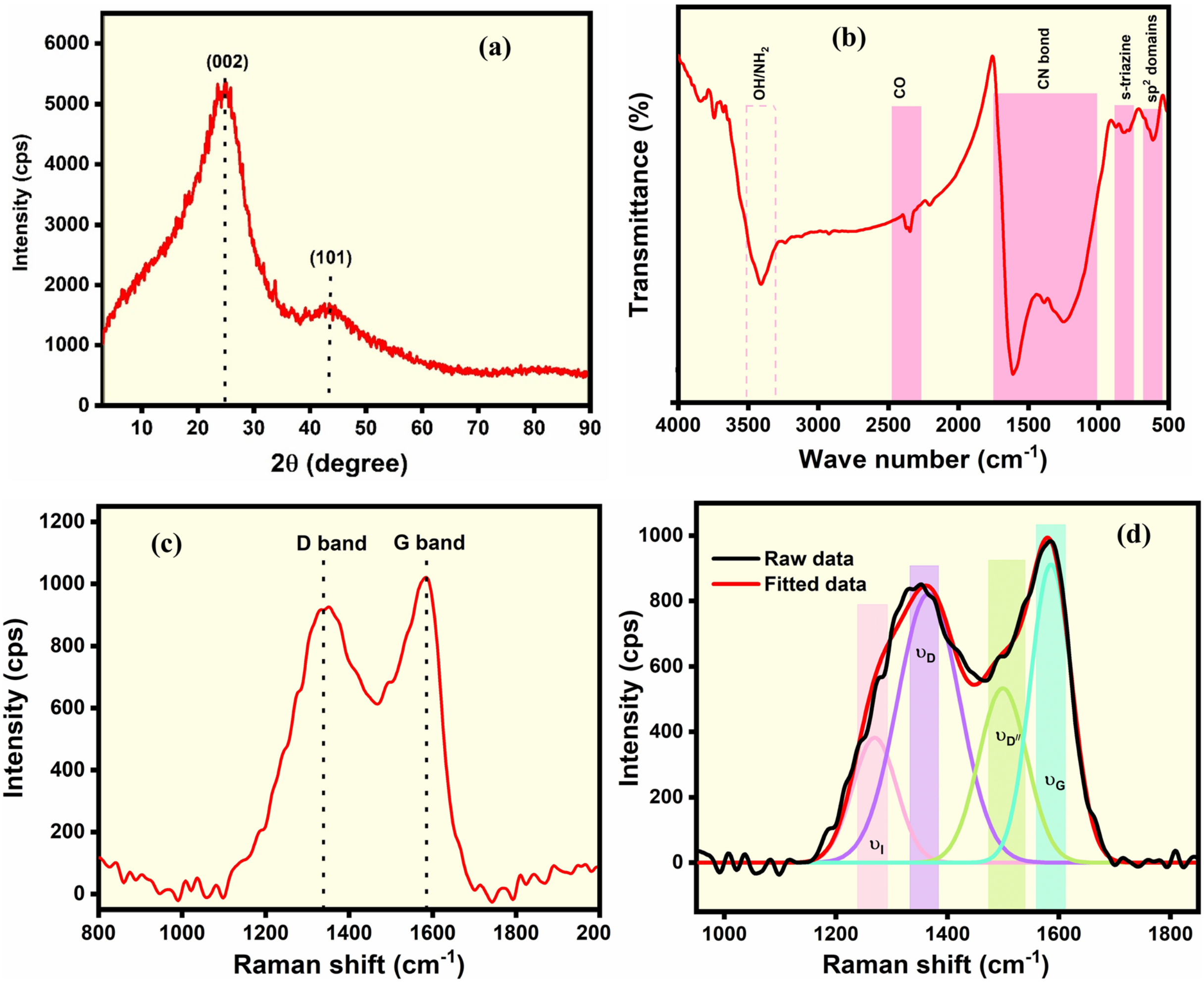

Fig. 1 (a) Powered X-ray diffraction pattern, (b) FT-IR, (c) Raman and (d) deconvoluted Raman spectra of mg-CN.

broadness of (002) peak indicates the formation of nanostructured mg-CN with poor crystallinity. While the peak corresponding to amorphous carbon is due to residual carbon arising from carboxymethyl cellulose (CMC) during carbonisation. The low intensity of the (101) peak suggests that the amorphous carbon is in a partially disordered arrangement.[27,28] It is worth mentioning that the presence of amorphous carbon in the frameworks of mg-CN is expected to increase the interlayer separation between the g-CN sheets, thereby facilitating facile charge storage by diffusion. The bulk chemical composition of the as-prepared mg-CN is investigated by FTIR analysis and the result is presented in Fig. 1b. The broad band around 3000–3400 cm^{-1} is associated with –NH and –OH stretching, which originates from terminal $–NH_2$ groups and adsorbed water.[29,30] The low-intensity peaks observed around 3800 cm^{-1} are attributed to the stretching vibrations of isolated –OH groups.[31] The strong peaks between 1200 and 1650 cm^{-1} correspond to C–N and C═N stretching vibrations, whereas the absorption band near 810 cm^{-1} is attributed to the out-of-plane bending of heptazine rings, typical of the g-CN framework.[32] The band observed in the FT-IR spectrum of mg-CN at around 606 cm^{-1} is attributed to the presence of sp^2 domains in amorphous carbon, which further confirms the presence of amorphous carbon domains.[20,33] To further study the nature and degree of graphitisation in the mg-CN, Raman spectroscopy is utilised. The Raman spectrum presented in Fig. 1c displays two prominent peaks at approximately 1353 cm^{-1} (D band) and 1588 cm^{-1} (G band), which are characteristic of disordered carbon and graphitic domains, respectively. Based on the literature report, the Raman spectrum was deconvoluted into four Gaussian bands, namely, *I*, D, D″ and G (Fig. 1d). The *I* and D bands represent disordered carbon, whereas D″ and G bands represent amorphous carbon and sp^2 graphitic carbon, respectively.[34,35] The ratio I_D/I_G of 1.87 obtained from the deconvoluted Raman spectrum indicates that mg-CN exhibits a relatively high degree of structural disorder and defect, which could have arisen during the thermal decomposition of the CMC. These defects, in combination with sp^2 carbon domains, could create additional electrochemically active sites for ion adsorption and redox reactions, thereby leading to enhanced specific capacitance and high rate capability.[36,37]

The surface chemical composition of the as-prepared mg-CN is investigated by recording X-ray photoelectron spectroscopy (XPS) and the results are presented in Fig. 2a–c. The survey spectrum shown in Fig. 2a displays peaks corresponding to C and N with relative atomic weights of 75.13 and 17.02%. Besides, oxygen-based functionalities originating from the decomposition of CMC and/or adsorbed water are witnessed as

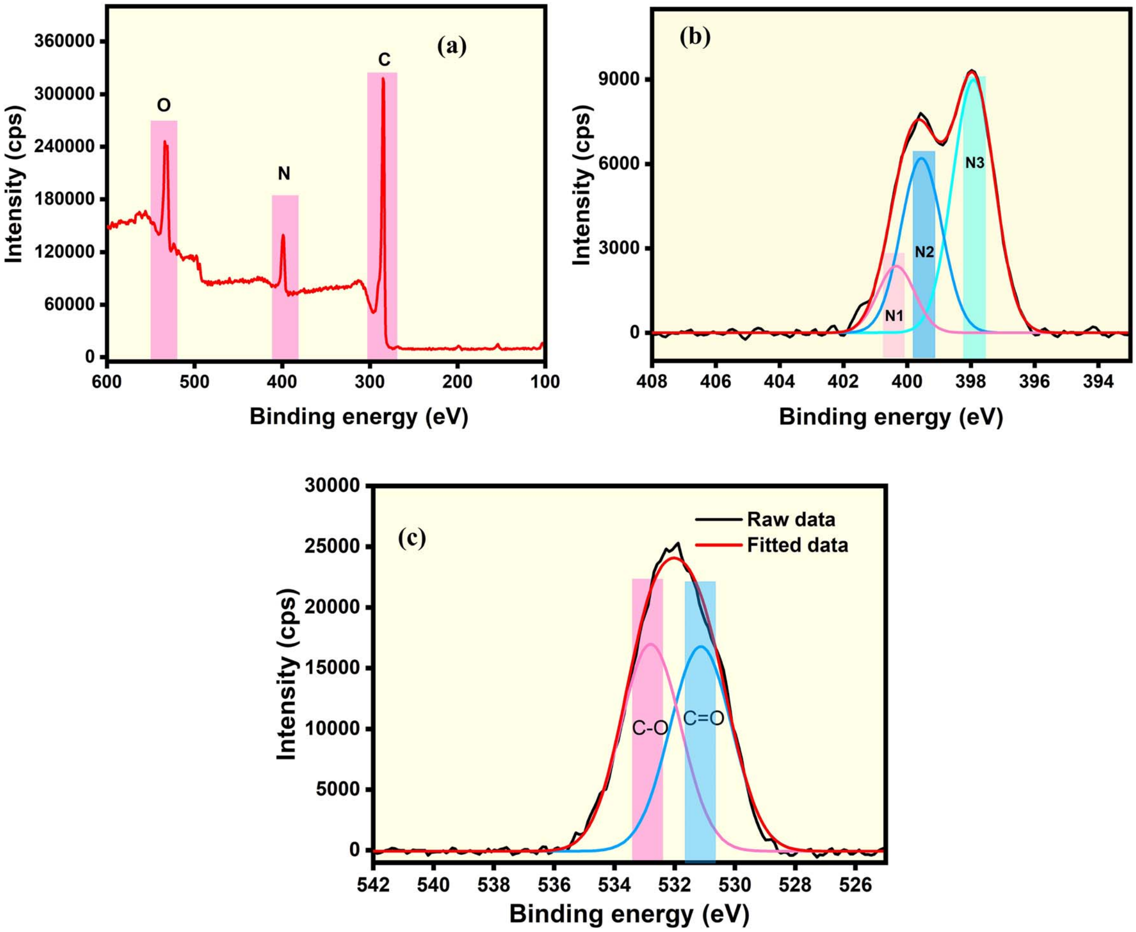

Fig. 2 (a) Survey and deconvoluted (b) N 1s, and (c) O 1s core level spectra of mg-CN.

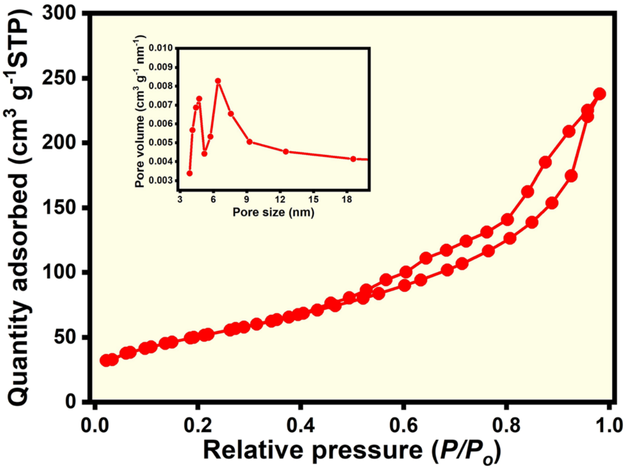

Fig. 3 N_2 sorption isotherms of mg-CN with BJH pore size distribution as an inset.

a peak in the survey spectrum of mg-CN (relative atomic weight of O = 7.85%). The relative atomic weight of nitrogen content obtained in the present is significantly lower than the value expected for ideal g-CN, which is attributed to the incomplete polycondensation of precursors and the presence of residual carbon originating from the thermal decomposition of CMC. Furthermore, the strong oxidising power of O could have resulted in the loss of N in the form of its oxides, leading to a lower relative atomic percentage of N. The high-resolution N 1s core level spectrum presented in Fig. 2b was deconvoluted into three distinct peaks assigned to terminal nitrogen in NH_2, nitrogen trigonally bonded to three carbon and nitrogen bonded to sp^2 carbon.[38,39] Furthermore, the deconvoluted high-resolution O 1s core level spectrum reveals the presence of C–O and C=O[40] (Fig. 2c). While pyridinic nitrogen is known to provide faradaic active sites and facilitate proton-coupled electron transfer, C=O contribute to redox-mediated charge storage.

The textural properties of the as-prepared mg-CN are evaluated by recording the nitrogen adsorption–desorption isotherm, and the results are presented in Fig. 3. The N_2 isotherm exhibits a type IV isotherm with type H3 hysteresis loop, indicating the presence of mesopores.[41] The steep uptake at relative pressures (P/P_0) above 0.4 suggests a hierarchical porous network with interparticle voids. The surface area and pore volume of mg-CN, derived from the desorption isotherm using the Brunauer–Emmett–Teller (BET) method, were found to be 139 m^2 g^{-1} (ref. 1) and 0.41 cm^3 g^{-1},[1] respectively. The inset Barrett–Joyner–Halenda (BJH) pore size distribution reveals that the pore size in the mg-CN is centred around ~5–8 nm.

Fig. 4a and b presents the TEM images of mg-CN recorded at both low and high resolution. The low-magnification TEM image (Fig. 4a) exhibits thin, wrinkled nanosheets with partially transparent regions, indicating a layered graphitic structure with reduced bulk density. At higher magnification (Fig. 4b), the nanosheets display a turbostratic stacking with interlayer voids, suggesting the successful introduction of mesoporosity through

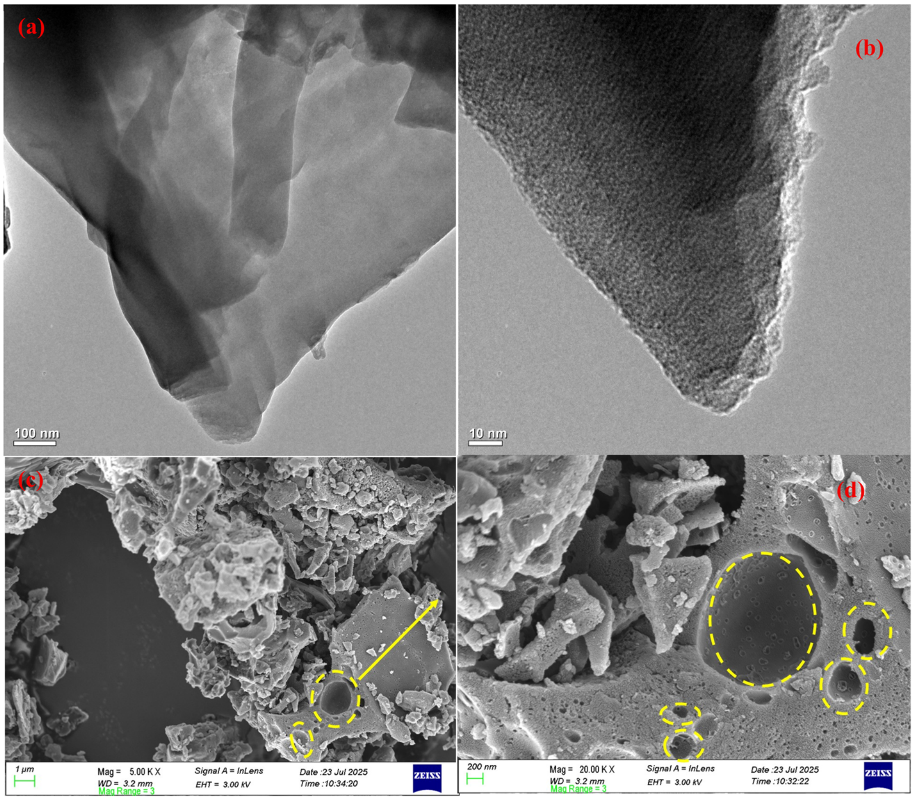

Fig. 4 (a) TEM, (b) high resolution TEM, (c) low and (d) high magnification FE-SEM images of mg-CN.

CMC-assisted templating. To further study the morphology of mg-CN, FE-SEM images were recorded and are presented in Fig. 4c and d. The low-magnification FE-SEM image (Fig. 4c) reveals an interconnected porous framework, while the high-magnification image (Fig. 4d) highlights the presence of surface pores. The surface porosity observed in the FE-SEM image of mg-CN is believed to originate from the decomposition of CMC during the thermal treatment under limited air. Indeed, hierarchical porous structures and interconnected networks in mg-CN are anticipated to facilitate the rapid transport of redox additives, thereby improving the rate performance.[42]

3.2 Characterization of 1 M H_2SO_4 + PVA and 1 M H_2SO_4 + PVA + 0.01 M HQ

Fig. 5a presents the SEM image of 1 M H_2SO_4 + PVA gel electrolyte, which exhibits a compact, fibrillar texture with limited mesoscopic porosity, typical of partially crystalline PVA. Upon the introduction of 0.01 M HQ, the surface becomes more corrugated with cavities and interstitial channels (Fig. 5b). The change in the morphology with the addition of HQ is ascribed to greater swelling of the PVA frameworks during gelation offered by HQ.[12] The DSC thermogram presented in Fig. 5c indicates that both gels demonstrate a low-temperature endotherm attributed to the loss of free water and plasticised PVA glass transition.[43] It can be observed that HQ-containing gel electrolyte shows a substantially larger endothermic peak, which could be due to the disruption of PVA crystallinity by HQ moieties. The endothermic peaks witnessed in the DSC graph of both electrolytes at around 220–240 °C are associated with the onset of thermal degradation of the PVA matrix.[44] Interestingly, this peak is found to shift to higher temperature in HQ-containing gel electrolyte, an indication that the presence of the HQ improves the thermal stability of PVA. The ionic conductivity of both electrolytes is determined using the EIS technique, and the

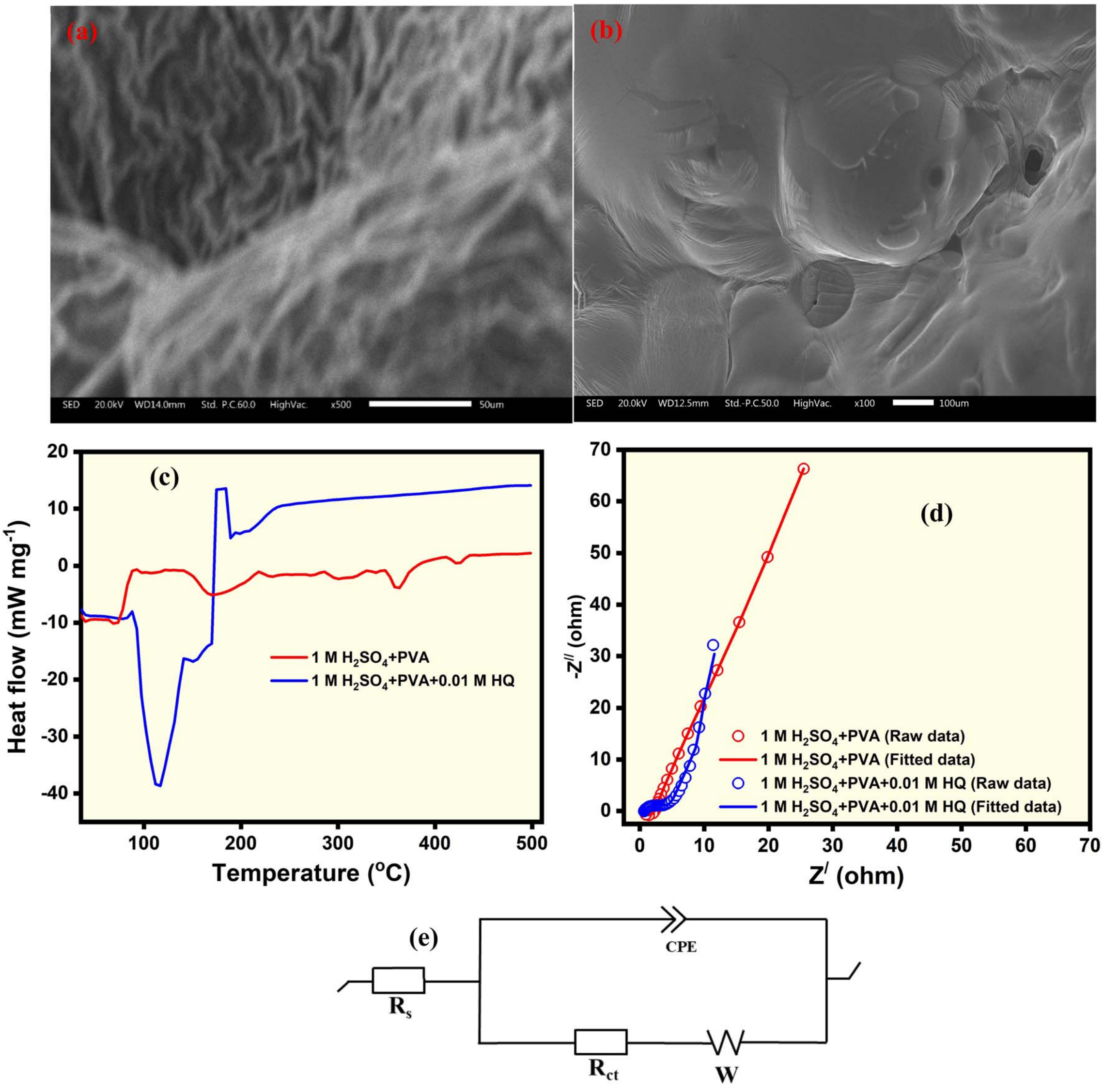

Fig. 5 SEM image of (a) 1 M H_2SO_4 + PVA and (b) 1 M H_2SO_4 + PVA + 0.01 M HQ. (c) DSC thermogram and (d) EIS spectra and (e) equivalent circuit used for fitting the EIS spectra of 1 M H_2SO_4 + PVA and 1 M H_2SO_4 + PVA + 0.01 M HQ.

Nyquist plots are presented in Fig. 5d. The equivalent circuit used for fitting the spectra is shown in Fig. 5e. It can be observed that the ionic conductivity of 1 M H_2SO_4 + PVA gel electrolyte of 371.44 mS cm^{-1} increased to 401.81 mS cm^{-1} with the addition of HQ. The observed increase in ionic conductivity is ascribed to the increase in concentration of charge carriers originating from HQ.[45,46] The enhancement in ionic conductivity upon the addition of 0.01 M HQ can be attributed to the combined effects of increased charge-carrier density and polymer-network plasticization.[47] While the participation of HQ in proton-coupled redox transitions increases the concentration of charge-carrier species, the disruption of intermolecular hydrogen bonding within the PVA matrix leads to a partial reduction in local crystallinity and improved segmental dynamics, which facilitates ion transport. It is worth mentioning that using a higher concentration of HQ results in the over-plasticization of the polymer, thereby weakening the gel network and reducing ion-pathway continuity.[48] To mitigate this, a low concentration of HQ is used in the present study.

3.3 Electrochemical studies of mg-CN in a three-electrode configuration

Redox electrolytes with various concentrations of HQ ranging from 0.005 M to 0.03 M in 1 M H_2SO_4 were prepared and screened based on their ionic conductivity using an Orion Star A329 Multipurpose Meter. Although 1 M H_2SO_4 exhibit the highest ionic conductivity, the ionic conductivity of redox additive electrolyte increases with an increase in the concentration of HQ up to 0.01 M and then decreases (Table 1). The highest ionic conductivity of 1 M H_2SO_4 is attributed to its large concentration of freely mobile protons and efficient proton transport *via* the Grotthuss mechanism.[49] On the other hand, the addition of a very small amount of hydroquinone (0.005 M) could have resulted in the formation of HQ/protonation equilibria, which can transiently reduce the population of freely mobile protons, thereby leading to a slight reduction in ionic conductivity.[49,50] It is worth mentioning that at a low concentration of 0.005 M HQ, the contribution of redox-active species to the total number of mobile charge carriers is minimal, and thus cannot compensate for the reduction in proton mobility. The increase in ionic conductivity at 0.01 M HQ is attributed to additional mobile redox species and enhanced proton-coupled electron transfer, thereby increasing the density of charge carriers. Therefore, it is plausible to state that the contribution of redox-active species to the total number of mobile charge carriers is sufficient to compensate for the reduction in proton mobility and produce a net increase in conductivity. At a higher concentration of 0.03 M, the observed decrease in the ionic conductivity is mainly due to self-association of HQ, leading to the settling of the undissolved HQ. Therefore, 0.01 M HQ is considered the optimal concentration of HQ.

Table 1 The ionic conductivity of 1 M H_2SO_4 and redox additive electrolyte with various concentrations of HQ

Electrolyte	Ionic conductivity (mS cm^{-1})
1 M H_2SO_4	188.9
0.005 M HQ + 1 M H_2SO_4	184
0.01 M HQ + 1 M H_2SO_4	186.8
0.03 M HQ + 1 M H_2SO_4	183.7

Fig. 6a shows the CVs of mg-CN recorded at a scan rate of 5 mV s^{-1} in 1 M H_2SO_4 and 1 M H_2SO_4 + 0.01 M HQ. The CV of mg-CN in 1 M H_2SO_4 electrolyte exhibits a quasi-rectangular profile, an indication of capacitance contribution from the accumulation of charges at the electrode/electrolyte interface and surface redox reaction of pyridinic and oxygen-based functionalities.[22] Upon the introduction of a small amount of benzoquinone corresponding to 0.01 M into 1 M H_2SO_4, well-defined redox peaks were observed in the CV of 1 M H_2SO_4 + 0.01 M HQ at 0.380 and 0.171 V, respectively. In general, the addition of benzoquinone to 1 M H_2SO_4 results in the formation of hydroquinone. Subsequently, the formed hydroquinone undergoes oxidation to benzoquinone during forward scan and reduces to hydroquinone during reverse scan, leading to the transfer of two electrons (eqn (5)).[45,46] Therefore, the observed redox peaks in the CV 1 M H_2SO_4 + 0.01 M HQ are attributed to the oxidation of hydroquinone to benzoquinone and the reduction of benzoquinone to hydroquinone. Owing to the redox shuttling, the area under the CV profile of 1 M H_2SO_4 + 0.01 M HQ is significantly higher than that of 1 M H_2SO_4, suggesting that mg-CN exhibits higher specific capacitance in 1 M H_2SO_4 + 0.01 M HQ than in 1 M H_2SO_4 electrolyte.

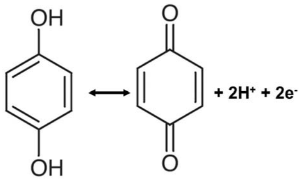

(5)

Fig. 6b and c depict the CVs of the mg-CN electrode recorded at various scan rates in 1 M H_2SO_4 and 1 M H_2SO_4 + 0.01 M HQ electrolytes, respectively. Although the mg-CN electrode exhibits an increase in current response with an increase in the scan rate in both electrolytes, a deviation from the quasi-rectangular shape is significantly observed in 1 M H_2SO_4 + 0.01 M HQ. The significant deviation from quasi-rectangular shape witnessed in the CV profile of mg-CN in 1 M H_2SO_4 + 0.01 M HQ is mainly attributed to the inherent sluggish reaction kinetics of benzoquinone/hydroquinone transformation. Furthermore, the unsustainability of the redox reaction at higher scan rates results in the inaccessibility of some active sites to the electrolyte ions and the limited diffusion effect of protonic ions.[51] Additionally, the increase in the diffusion resistance of electrolyte ions at higher scan rates results in the shift of redox peaks towards higher potentials and broadening of peak areas in the CVs of the mg-CN electrode in 1 M H_2SO_4 + 0.01 M HQ electrolyte.[52]

To understand the prevailing process contributing to the overall capacitance in both electrolytes, the Dunn method is utilised.[53]

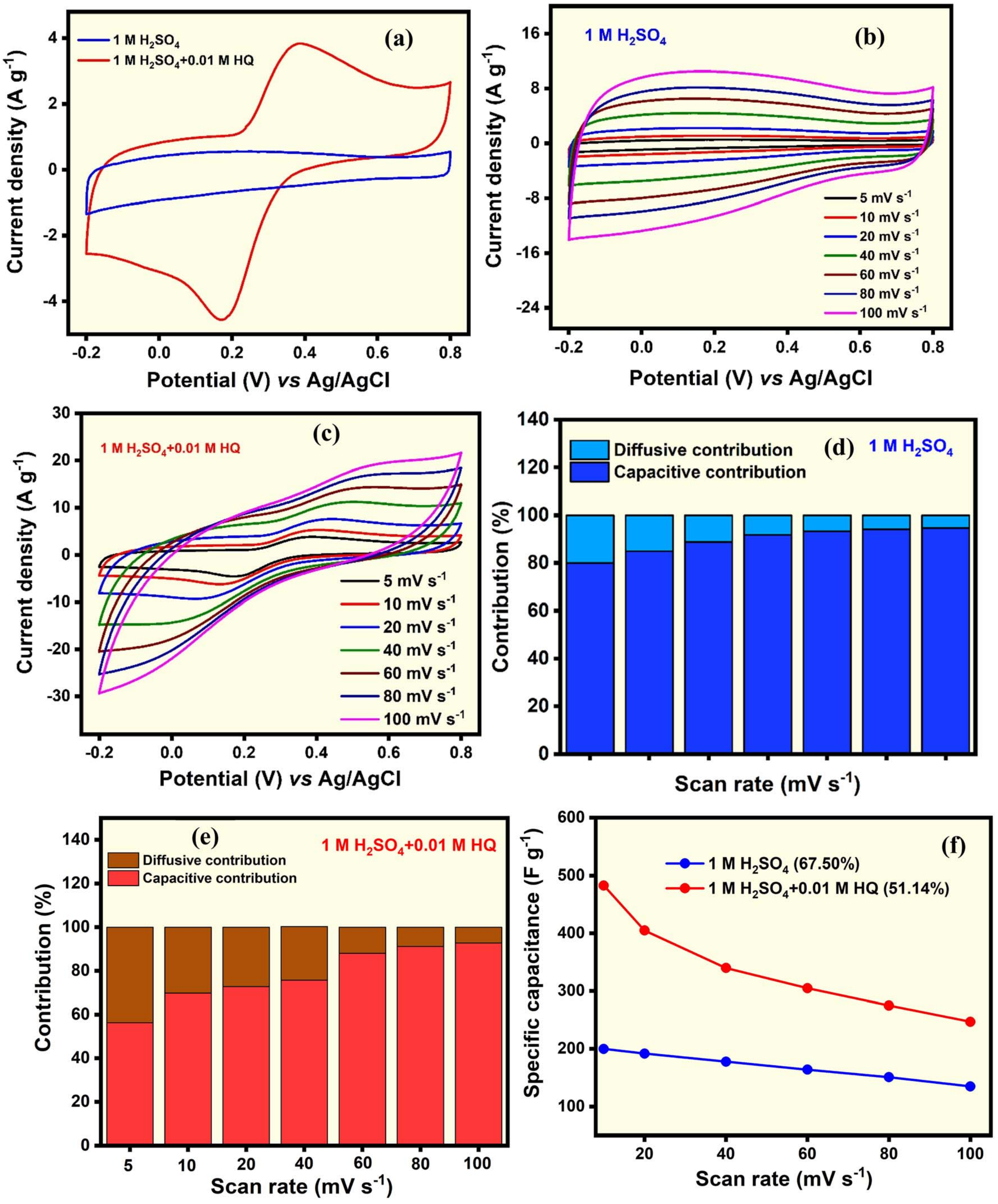

Fig. 6 (a) CV of mg-CN recorded at a scan rate of 5 mV s^{-1} in M H_2SO_4 and HQ-based electrolyte. CVs of mg-CN recorded at various scan rates in 1 M H_2SO_4 (b) and HQ-based electrolyte (c). Percentage capacitance contribution in 1 M H_2SO_4 (d) and HQ-based electrolyte (e). Rate performance of mg-CN in both electrolytes (f).

$$i(v) = k_1 v + k_2 v^{1/2} \tag{6}$$

$$\frac{i(v)}{v^{1/2}} = k_1 v^{1/2} + k_2 \tag{7}$$

where v and i denote the scan rate (mV s^{-1}) and current density (mA g^{-1}), k_1 and k_2 are the slope and intercept of the linear fit of $\frac{i(v)}{v^{1/2}}$ *vs.* $v^{1/2}$, respectively. After determining the slope and intercept, the percentage capacitive and diffusive contributions are calculated using eqn (8) and (9).

$$\text{Percentage capacitive contribution} = \frac{k_1 v}{k_1 v + k_2 v^{1/2}} \times 100\% \tag{8}$$

$$\text{Percentage diffusive contribution} = 100 - \text{capacitive contribution} \tag{9}$$

Fig. 6d and e represent the percentage contribution of capacitive and diffusion-controlled processes, as estimated using eqn (8) and (9). Evidently, a diffusion-controlled process contributes up to 42.71% in the HQ-based electrolyte at a scan rate of 5 mV s^{-1}, which is approximately two-fold higher than that of 1 M H_2SO_4. Nonetheless, the percentage capacitive contribution increases with an increase in the scan rate and becomes a dominant process at high scan rates. It is worth mentioning that the diffusive-controlled process still contributes to the overall capacitance of the HQ-based electrolyte even at a scan rate of 100 mV s^{-1}, underscoring the rapid and reversible redox kinetics facilitated by the hierarchical porous structure of the mg-CN electrode.

The specific capacitance of mg-CN in both electrolytes is further calculated by using eqn (10).[54]

$$\mathrm{SC} = \frac{1}{m_\mathrm{e} v}\int_{V_1}^{V_2} I\mathrm{d}V \tag{10}$$

where SC, m_e, v, and $\int_{V_1}^{V_2} I\mathrm{d}V$ are the specific capacitance (F g^{-1}), mass of the electroactive materials (g), scan rate (mV s^{-1}) and integrated area enclosed under the CV curve, respectively. As depicted in Fig. 6f, mg-CN delivers an SC of 481 F g^{-1} at a scan rate of 5 mV s^{-1} in HQ-based electrolyte as compared to 198 F g^{-1} obtained in a 1 M H_2SO_4 system at the same scan rate. The higher value of SC in the HQ-based system is attributed to the redox chemistry of benzoquinone.[55,56] Owing to the decrease in the SC from the diffusion-controlled process at higher scan rates, the mg-CN electrode exhibits better rate performance in a 1 M H_2SO_4 electrolyte.

3.4 Capacitance studies of symmetrical supercapacitor devices using redox-mediated additive electrolyte

Fig. 7a depicts the CV of the devices fabricated using 1 M H_2SO_4 + PVA (PVA) and 1 M H_2SO_4 + PVA + 0.01 M HQ (PVA–HQ) electrolyte recorded at a scan rate of 5 mV s^{-1}. The CV curve of the device in PVA electrolyte shows a near-rectangular CV indicative of double-layer capacitive and pseudocapacitive behaviour. Upon introducing 0.01 M hydroquinone (HQ), the area under the CV increased, and a humps-like feature appeared, a characteristic feature of the fast and reversible reaction originating from the HQ/BQ couple shuttling.[57,58] The higher area enclosed under the CV profile of the device in the PVA–HQ system suggests that it has better electrochemical performance as compared to the PVA system. The enhancement

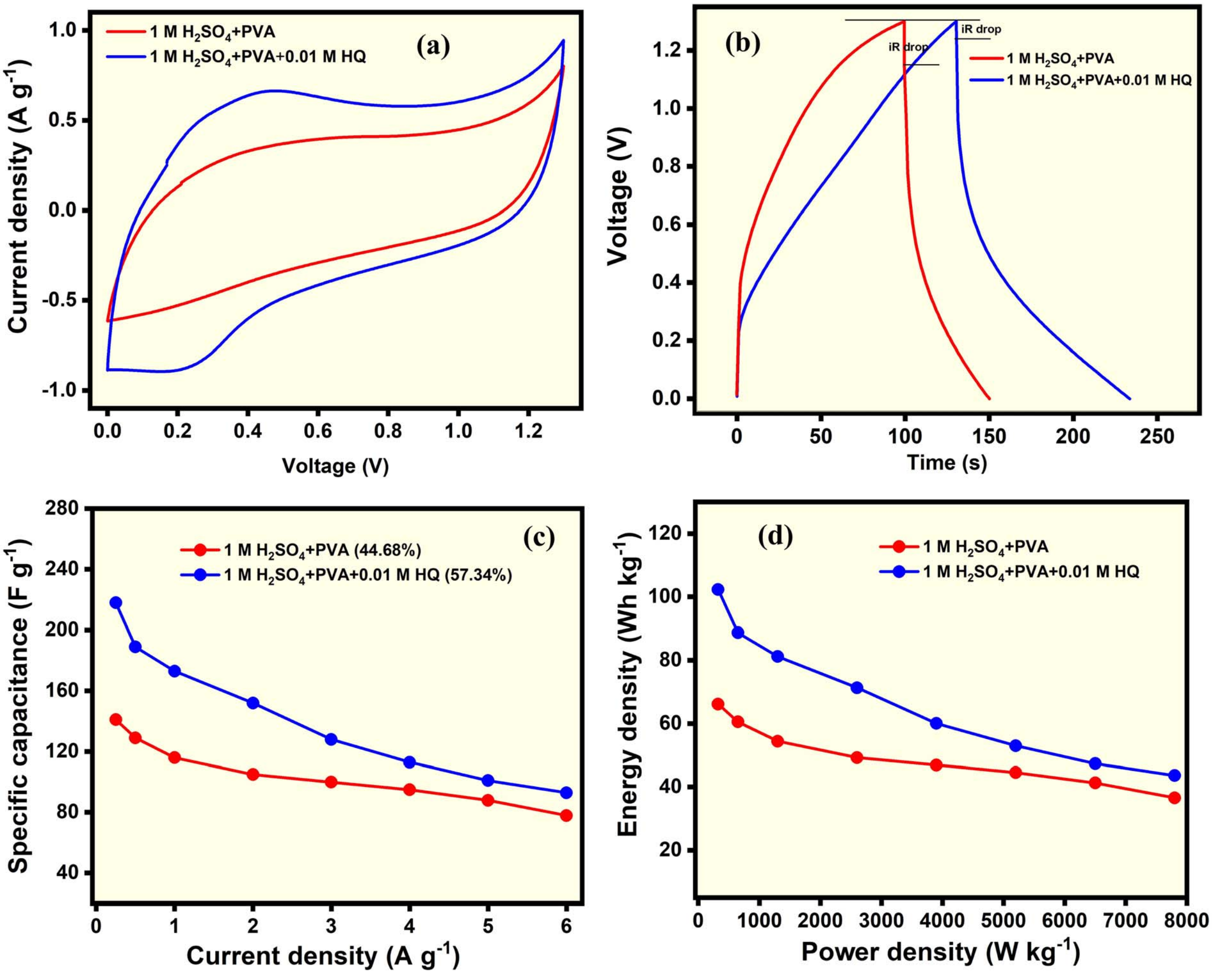

Fig. 7 (a) CV of symmetrical device recorded at a scan rate of 5 mV s^{-1}, (b) GCD curve recorded at current density of 0.5 A g^{-1}, (c) rate performance and (d) Ragone plot of symmetrical devices in 1 M H_2SO_4 + PVA and 1 M H_2SO_4 + PVA + 0.01 M HQ.

in the capacitance of the device in PVA–HQ electrolyte is attributed to the pseudocapacitance arising from the HQ/BQ couple.[58,59] Fig. 7b shows the galvanostatic charge–discharge (GCD) curve of the devices recorded at a current density of 0.5 A g^{-1}. It can be observed that the GCD profile of the device in both electrolytes exhibits a quasi-symmetrical shape, further suggesting that the devices store charges through both mechanisms. Although the GCD profiles of the devices are similar, the supercapacitor device fabricated using PVA/HQ electrolyte exhibits a longer discharge time and a smaller IR drop. The longer discharge time of the device in PVA/HQ systems indicates the higher charge storage capability, whereas the lower IR drop suggests a lower equivalent series resistance.[54] Quantitatively, a supercapacitor device fabricated using PVA/HQ electrolyte delivers a SC of 218 F g^{-1} at a current density of 0.25 A g^{-1}, compared to the PVA system, which delivers a specific capacitance of 141 F g^{-1} at the same current density. When the current density is increased from 0.25 to 6 A g^{-1}, the devices in both electrolytes exhibit a gradual decrease in the SC value (Fig. 7c). While the progressive decrease in the SC with an increase in current density is attributed to increases in the diffusive resistance to the transport of the electrolyte ions at higher discharge current density, the better rate retention of the device in PVA/HQ system could be attributed to higher ionic conductivity of the gel offers by the charge carriers originating from the HQ (Fig. 5d).[60,61] Fig. 7d presents the energy density and power density of the device in both electrolytes. According to eqn (3) and (4), the energy density of the device is calculated to be 88.73 and 60.56 Wh kg^{-1} at a power density of 650 W kg^{-1} in the PVA/HQ and PVA systems, respectively, representing a 1.46-fold increase. Moreover, when the power density is increased to 6500 W kg^{-1}, which corresponds to a ten times increment, the device in PVA/HQ still delivers an energy density of 47.42 Wh kg^{-1}, an indication that the PVA/HQ electrolyte can be employed for the fabrication of a high-rate supercapacitor. It is worth mentioning that the energy density obtained in the present study surpasses the values reported in the literature (Table 2).

The electrochemical impedance spectroscopy (EIS) is utilised to understand the capacitive and diffusive behaviour of mg-CN in both 1 M H_2SO_4 + 0.01 M HQ under a three-electrode configuration and 1 M H_2SO_4 + PVA + 0.01 M HQ under two-electrode configurations. Fig. 8 presents the Bode plot of mg-CN recorded in both electrolytes. The lower value of the Bode magnitude of mg-CN in the redox additive electrolyte (1.45 Ω) as compared to the redox gel polymer electrolyte (device, 2.70 Ω) indicates that mg-CN exhibits lower resistance in the redox electrolyte. On the other hand, the higher phase angle response of the two-electrode system (68.91°) as compared to the three-electrode system (54.05°) suggests that the surface-controlled process is the predominant charge storage mechanism in the device.[62] The predominantly surface-controlled process in the device could be attributed to the higher resistance, which has slowed the facile ion transport and thus suppressed the capacitance contribution from the redox reaction involving the HQ/BQ couple.[62] It is worth mentioning that the device failed during practical testing. Although the exact cause of the failure is not yet known, it could be attributed to several factors, including current leakage, internal resistance and contact instability. Partial gel shrinkage could have weakened the electrode/electrolyte interface, thereby increasing the internal resistance of the device. While the contact instability between the electrode surface/gel electrolyte and stainless-steel current collectors may disrupt the electron/ion transfer interface, leakage current arising from side reactions could have depleted the charge stored in the device. The above-mentioned factors could have caused the device to fail during the practical testing.

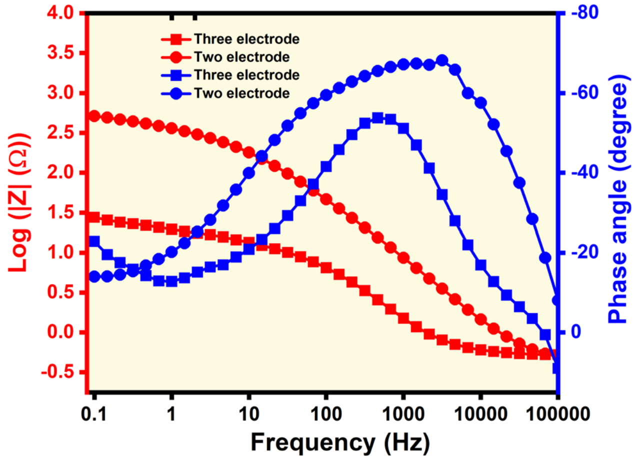

Fig. 8 Bode plot of EIS spectra mg-CN recorded in 1 M H_2SO_4 + 0.01 HQ electrolyte under three three-electrode configurations (labelled as: three electrode) and 1 M H_2SO_4 + 0.01 HQ + PVA electrolyte for the device (labelled as: two electrode).

Table 2 Comparative energy and power density obtained in the present study with other carbonaceous materials in the redox additive electrolyte

Material	Electrolyte	Energy density (Wh kg^{-1})	Power density (W kg^{-1})	Reference
mg-CN	PVA + H_2SO_4 + HQ	47.42	6500	Present study
ZnO/NiO@MWCNT	$NaSO_4$ + $K_4[Fe(CN)_6]$	43.59	4000	64
Nanoporous carbon	Na_2MoO_4 + KI	65.3	1500	65
Reduced graphene oxide	K_2SO_4 + $K_3Fe(CN)_6$	36.8	1200	66
S-doped graphene	H_2SO_4 + Hydroquinone	27.00	810	66
Activated carbon	PVDF-HFP/SN/BMPTFSI + HQ	40.00	20 000	67

Cycling stability and voltage holding are important parameters used to evaluate the performance of a supercapacitor. Hence, a symmetrical device fabricated using PVA/HQ electrolyte is subjected to continuous charge–discharge cycling at a current density of 3 A g^{-1}, and the result is presented in Fig. 9c. Evidently, the device retains nearly constant specific capacitance with coulombic efficiency reaching ≈100%, an indication of the excellent stability of the electrolyte and robust reversibility of the HQ couple in the gel. Furthermore, the device was subjected to GCD cycling (4 cycles) followed by 2 hours of voltage holding after the last charge and 2 hours of voltage holding after the last discharge cycles (Fig. 9a). As depicted in Fig. 9b, the device demonstrates excellent stability.[63]

To understand the structural durability of mg-CN, post-cycling morphological analysis is conducted. After the device was subjected to continuous cycling at a current density of 3 A g^{-1} in PVA/HQ electrolyte, it was disassembled, and the electrodes were washed with deionised water and then dried in an oven. The electrode material was carefully scraped from the SS foil, and SEM images were recorded. As seen in Fig. 10, the SEM images of the electrode revealed that the nanosheet-derived porous framework and interconnected architecture of mg-CN are largely preserved, indicating structural integrity. On the other hand, a slight surface smoothing is noticeable, which could be attributed to the repeated proton insertion/extraction.[68] It is worth noting that the post-cycling analysis did not provide information on the degradation mechanism of the PVA/HQ electrolyte. In general, HQ undergoes a reversible two-electron, two-proton redox transformation with benzoquinone (BQ). However, under prolonged cycling, secondary side reactions may compete with the reversible HQ/BQ shuttle, particularly when confined in PVA.[69] At elevated overpotentials, this is expected to result in irreversible oxidation of HQ to polymeric quinone species *via* radical-mediated coupling.[70] Owing to decreased redox reaction resulting from the formation of these polymeric products, the pseudocapacitive contribution decreases over time. Furthermore, during continuous cycling, proton depletion may induce pH shifts within the gel matrix, thereby pushing the equilibrium toward partially oxidised intermediates, resulting in a decrease in the specific capacitance.[71]

Although the device performed well in laboratory electrochemical testing, the cell failed to power an LED. This failure can be attributed to several likely mechanisms. First, gel polymer electrolytes containing PVA are prone to gradual moisture loss, which leads to shrinkage and weakening of the electrode–gel interface, resulting in loss of ionic contact. Second, prolonged operation of HQ/BQ-based redox electrolytes can lead to

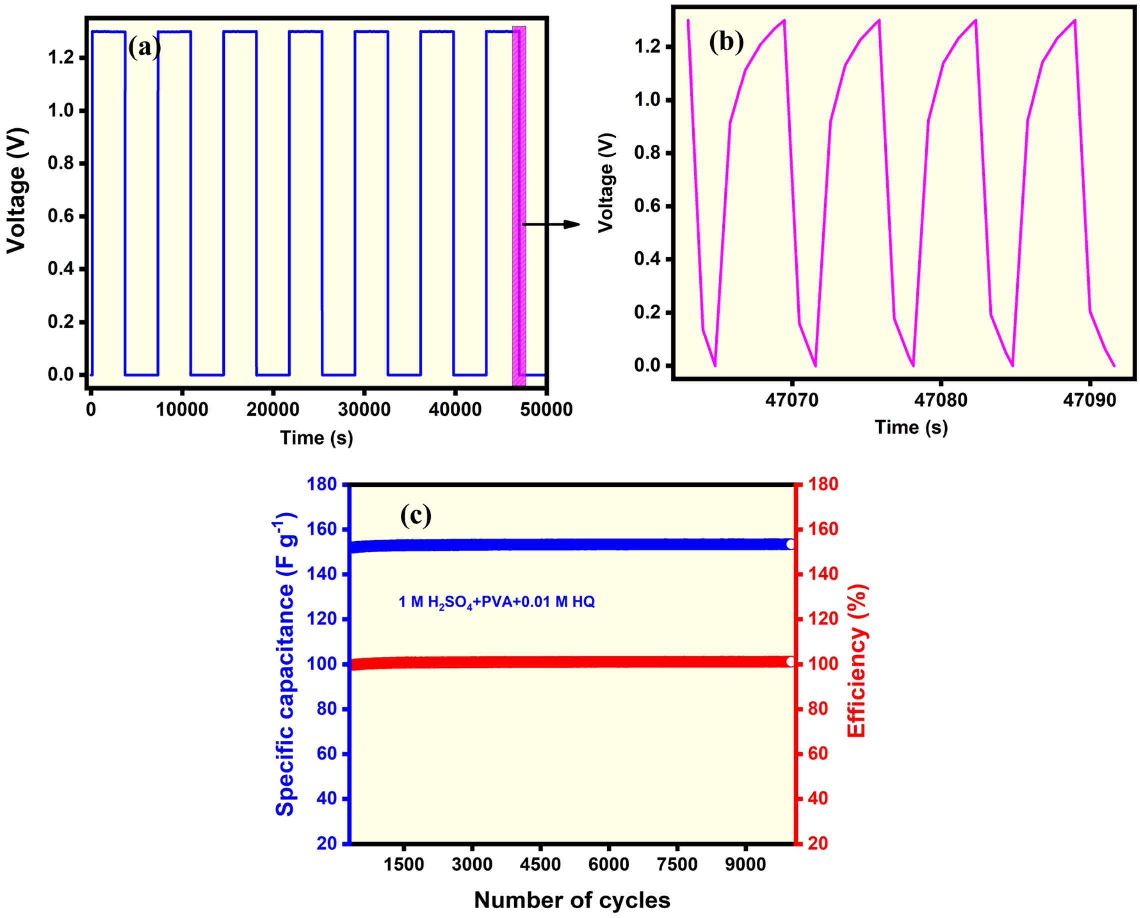

Fig. 9 (a) Voltage holding, (b) GCD after voltage holding, (c) cycling stability recorded at the current density of 3 A g^{-1} in PVA + 1 M H_2SO_4 + 0.01 HQ system.

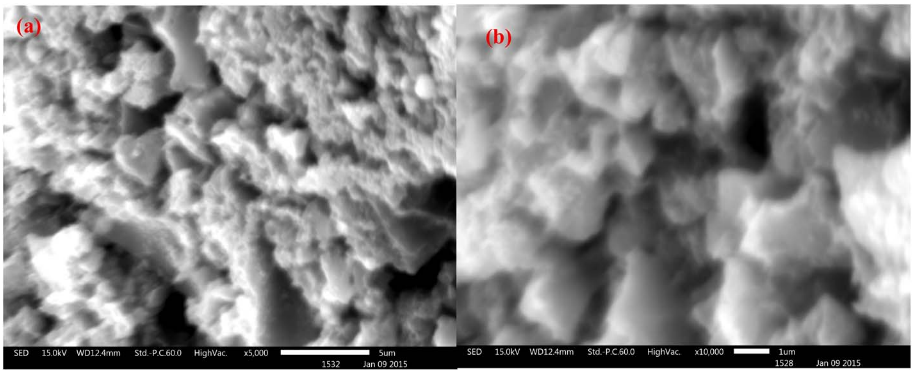

Fig. 10 (a) Low and (b) high magnification SEM images of the mg-CN electrode after continuous GCD cycling at the current density of 3 A g^{-1}.

local concentration imbalances or partial redox shuttle degradation, reducing the reversibility of the redox-mediated charge storage process. Third, repeated bending or minor mechanical disturbance of the gel layer during device assembly and handling may induce micro-cracks within the gel, increasing internal resistance and eventually disrupting electron–ion transport pathways. These effects are consistent with failure modes reported for other redox-mediated gel systems and explain the practical breakdown observed in this study.

4 Conclusion

This study present a rational approach to enhance the supercapacitive performance of mg-CN. The mg-CN synthesised *via* a green templating route offered abundant active sites and fast ion transport channels, which, when coupled with a hydroquinone-mediated gel polymer electrolyte, enabled dual charge storage mechanisms, namely, electric double-layer capacitance and pseudocapacitance. The integration of HQ not only improved ionic conductivity and thermal robustness but also significantly enhanced energy and power densities, delivering an energy density of 47.42 Wh kg^{-1} and outstanding rate capability. Moreover, the device exhibited excellent cycling stability. These findings highlight the promising potential of redox-mediated gel polymer electrolytes for fabricating high-rate supercapacitors.

Author contributions

Mustapha Balarabe Idris: conceptualization, data curation, formal analysis, investigation, validation, writing and editing. Bhekie B. Mamba: editing, funding acquisition, project administration, Fuku Xolile: editing, funding acquisition, project administration, resources, supervision, visualization, writing – review & editing.

Conflicts of interest

The authors declare that they have no known competing financial interests or personal relationships that could have appeared to influence the work reported in this paper.

Data availability

Data will be made available on request.

Acknowledgements

The authors would like to express their gratitude to the University of South Africa, the Institute for Nanotechnology and Water Sustainability (iNanoWS), College of Science, Engineering, and Technology for funding and research facilities. During the preparation of this work, the author(s) used Grammarly software for spelling, grammar, and punctuation checks. After using this tool, the author(s) reviewed and edited the content as needed and take(s) full responsibility for the content of the published article.

References

1 M. B. Idris, Z. Musa Mohammed, S. Nuhu, H. Aliyu, H. Abba, B. B. Mamba, D. Sappani and F. Xolile, *ACS Omega*, 2025, **10**, 18184–18212.
2 M. B. Idris, S. Nuhu, Z. M. Mohammed, H. Aliyu, H. Abba, F. Xolile and S. Devaraj, *J. Energy Storage*, 2024, **93**, 112322.
3 Y. A. Kumar, S. Vignesh, T. Ramachandran, K. D. Kumar, A. G. Al-Sehemi, M. Moniruzzaman and T. H. Oh, *J. Energy Storage*, 2024, **97**, 112826.
4 A. Kumar, B. N. Mahanty, A. Rawat, R. Muhammad, R. K. Panigrahi, D. Pradhan and P. Mohanty, *Energy Fuels*, 2023, **37**, 6810–6823.
5 N. Huang, Y. Sun, S. Liu, X. Wang, J. Zhang, L. Guo, J. Bi and X. Sun, *Small*, 2023, **19**, 2300696.
6 Y. Sun, G. Zhang, S. Tan, H. Wang, Y. Liu, C. Sun, B. Deng, K. Zhang, Z. Gao and N. Huang, *Chem. Eng. J.*, 2025, 165031.
7 Y. Sun, M. Ge, B. Xie, H. Zhang, Z. Gao, X. Zhao, B. Deng, K. Zhang, S. Zhang and C. Sun, *J. Energy Storage*, 2025, **133**, 118060.
8 Y. Sun, Y. Sheng, W. Jiang, C. Sun, X. Zhao, B. Deng, K. Zhang, Z. Gao, S. Zhang and X. Wang, *Vacuum*, 2024, **225**, 113218.
9 B. Akinwolemiwa, C. Peng and G. Z. Chen, *J. Electrochem. Soc.*, 2015, **162**, A5054.

10 K. W. Nam, C. W. Lee, X. Q. Yang, B. W. Cho, W. S. Yoon and K. B. Kim, *J. Power Sources*, 2009, **188**, 323–331.
11 G. Ma, E. Feng, K. Sun, H. Peng, J. Li and Z. Lei, *Electrochim. Acta*, 2014, **135**, 461–466.
12 S. Alipoori, S. Mazinani, S. H. Aboutalebi and F. Sharif, *J. Energy Storage*, 2020, **27**, 101072.
13 N. Ahmad, A. Rinaldi, M. Setti, M. Sidoli, S. Scaravonati, V. Vezzoni, G. Magnani, M. Riccò, C. Milanese and M.-M. Titirici, *ACS Appl. Energy Mater.*, 2025, **8**, 9391–9406.
14 J. Yang, M. Wang, T. Chen, X. Yu, G. Qin, X. Fang, X. Su and Q. Chen, *Sci. China Mater.*, 2023, **66**, 1779–1792.
15 B. Guan, Q. Y. Shan, H. Chen, D. Xue, K. Chen and Y. X. Zhang, *Electrochim. Acta*, 2016, **200**, 239–246.
16 Z. Li, L. Wu, L. Wang, A. Gu and Q. Zhou, *Electrochim. Acta*, 2017, **231**, 617–625.
17 L.-L. Zhang, S. Duan, X.-L. Yang, G. Liang, Y.-H. Huang, X.-Z. Cao, J. Yang, M. Li, M. C. Croft and C. Lewis, *J. Power Sources*, 2015, **278**, 826–827.
18 P. Wen, P. Gong, J. Sun, J. Wang and S. Yang, *J. Mater. Chem. A*, 2015, **3**, 13874–13883.
19 M. B. Idris, G. Sakthivel and S. Devaraj, *Mater. Today Energy*, 2018, **10**, 325–335.
20 M. B. Idris, G. H. Sai, D. Hemalatha, G. Sakthivel and S. Devaraj, *J. Electrochem. Soc.*, 2019, **166**, A2409–A2418.
21 M. B. Idris and S. Devaraj, *Electrochim. Acta*, 2019, **303**, 219–230.
22 M. B. Idris and S. Devaraj, *New J. Chem.*, 2019, **43**, 11626–11635.
23 M. B. Idris and D. Sappani, *Chemistryselect*, 2018, **3**, 11258–11269.
24 A. D. Shuaibu, S. S. Shah, A. S. Alzahrani and M. A. Aziz, *J. Energy Storage*, 2025, **107**, 114851.
25 E. Frackowiak, K. Metenier, V. Bertagna and F. Beguin, *Appl. Phys. Lett.*, 2000, **77**, 2421–2423.
26 B. E. Conway, *Electrochemical Supercapacitors: Scientific Fundamentals and Technological Applications*, Springer Science & Business Media, 2013.
27 M. B. Idris, T. Subramaniam and D. Sappani, *Diam. Relat. Mater.*, 2022, **129**, 109359.
28 M. Anbia and M. Haqshenas, *Int. J. Sci. Environ. Technol.*, 2015, **12**, 2649–2664.
29 W. Cha, I. Y. Kim, J. M. Lee, S. Kim, K. Ramadass, K. Gopalakrishnan, S. Premkumar, S. Umapathy and A. Vinu, *ACS Appl. Mater. Interfaces*, 2019, **11**, 27192–27199.
30 S. Joseph, D. M. Kempaiah, M. Benzigar, A. V. Baskar, S. N. Talapaneni, S. H. Jhung, D. H. Park and A. Vinu, *J. Mater. Chem. A*, 2017, **5**, 21542–21549.
31 H. Lin, J. Long, Q. Gu, W. Zhang, R. Ruan, Z. Li and X. Wang, *Phys. Chem. Chem. Phys.*, 2012, **14**, 9468–9474.
32 H. S. Gujral, G. Singh, J. H. Yang, C. I. Sathish, J. B. Yi, A. Karakoti, M. Fawaz, K. Ramadass, A. H. Al-Muhtaseb, X. J. Yu, M. B. H. Breese and A. Vinu, *Carbon*, 2022, **195**, 9–18.
33 B. Antil, L. Kumar, M. R. Das and S. Deka, *J. Energy Storage*, 2022, **52**, 104731.
34 F. Bonhomme, J. C. Lassegues and L. Servant, *J. Electrochem. Soc.*, 2001, **148**, E450–E458.
35 A. C. Ferrari, J. C. Meyer, V. Scardaci, C. Casiraghi, M. Lazzeri, F. Mauri, S. Piscanec, D. Jiang, K. S. Novoselov and S. Roth, *Phys. Rev. Lett.*, 2006, **97**, 187401.
36 A. G. Olabi, Q. Abbas, M. A. Abdelkareem, A. H. Alami, M. Mirzaeian and E. T. Sayed, *Batteries*, 2022, **9**, DOI: 10.3390/batteries9010019.
37 K. S. Kumar, N. Choudhary, Y. Jung and J. Thomas, *ACS Energy Lett.*, 2018, **3**, 482–495.
38 K. S. Lakhi, W. S. Cha, S. Joseph, B. J. Wood, S. S. Aldeyab, G. Lawrence, J.-H. Choy and A. Vinu, *Catal. Today*, 2015, **243**, 209–217.
39 K. S. Lakhi, D.-H. Park, K. Al-Bahily, W. Cha, B. Viswanathan, J.-H. Choy and A. Vinu, *Chem. Soc. Rev.*, 2017, **46**, 72–101.
40 D. H. Park, K. Lakhi, K. Ramadass, M. K. Kim and A. Vinu, *Abstr. Pap. Am. Chem. Soc.*, 2017, **23**, 10753–10757.
41 S. Gao, F. Liao, S. Ma, L. Zhu and M. Shao, *J. Mater. Chem. A*, 2015, **3**, 16520–16527.
42 K. Sun, F. Ran, G. Zhao, Y. Zhu, Y. Zheng, M. Ma, X. Zheng, G. Ma and Z. Lei, *RSC Adv.*, 2016, **6**, 55225–55232.
43 S. Scurti, J. Ortolani, A. Ghirri, E. Maccaferri, D. Caretti and L. Mazzocchetti, *Prog. Org. Coat.*, 2023, **177**, 107457.
44 G. D'Altri, L. Yeasmin, V. Di Matteo, S. Scurti, A. Giovagnoli, M. F. Di Filippo, I. Gualandi, M. C. Cassani, D. Caretti and S. Panzavolta, *ACS Omega*, 2024, **9**, 6391–6402.
45 S. Abbasi, F. Hekmat, S. Shahrokhian, M. Chougale and D. P. Dubal, *Small*, 2024, **20**, 2406467.
46 C. Singh and A. Paul, *J. Phys. Chem. C*, 2015, **119**, 11382–11390.
47 S. Alipoori, S. H. Aboutalebi and M. Barsbay, *J. Solid State Electrochem.*, 2024, **28**, 2643–2657.
48 A. Imbrogno, J. Islam, C. Santillo, R. Castaldo, L. Sygellou, C. Larrigy, R. Murray, E. Vaughan, M. K. Hoque, A. J. Quinn and D. Iacopino, *ACS Appl. Electron. Mater.*, 2022, **4**, 1541–1551.
49 G. Arumugam, B. Chettiannan, S. Mathan, M. Selvaraj, M. A. Assiri and R. Rajendran, *J. Energy Storage*, 2025, **121**, 116595.
50 L. Guan, L. Guo, H. Yao, J. Cai, X. Dong, R. Wang, Z. Zhai, X. Chen, X. Wei and D. Li, *Molecules*, 2025, **30**, 1764.
51 H. Yu, J. Wu, J. Lin, L. Fan, M. Huang, Y. Lin, Y. Li, F. Yu and Z. Qiu, *ChemPhysChem*, 2013, **14**, 394–399.
52 G. Rutavi, D. J. Tarimo, V. M. Maphiri, V. N. Kitenge, K. O. Otun, H. N. Mutua and N. Manyala, *J. Alloys Compd.*, 2025, **1037**, 182271.
53 L. Zhang, T. Wang, T.-N. Gao, H. Xiong, R. Zhang, Z. Liu, S. Song, S. Dai and Z.-A. Qiao, *CCS Chem.*, 2021, **3**, 870–881.
54 O. A. Akintayo, G. M. Al-Senani, S. A. Adewinbi, V. M. Maphiri, S. D. Al-Qahtani and N. Manyala, *J. Solid State Electrochem.*, 2025, 1–17.
55 H. Xie, Y. Zhu, Y. Wu, Z. Wu and E. Liu, *Mater. Res. Bull.*, 2014, **50**, 303–306.
56 R. Xu, F. Guo, X. Cui, L. Zhang, K. Wang and J. Wei, *J. Mater. Chem. A*, 2015, **3**, 22353–22360.
57 J. Zhong, L.-Q. Fan, X. Wu, J.-H. Wu, G.-J. Liu, J.-M. Lin, M.-L. Huang and Y.-L. Wei, *Electrochim. Acta*, 2015, **166**, 150–156.

58 P. Bharathidasan, M. B. Idris, D.-W. Kim, S. Sivakkumar and S. Devaraj, *FlatChem*, 2019, **15**, 100108.

59 H. Yu, J. Wu, L. Fan, K. Xu, X. Zhong, Y. Lin and J. Lin, *Electrochim. Acta*, 2011, **56**, 6881–6886.

60 Y. Zhu, E. Liu, Z. Luo, T. Hu, T. Liu, Z. Li and Q. Zhao, *Electrochim. Acta*, 2014, **118**, 106–111.

61 S. Senthilkumar, R. K. Selvan, Y. Lee and J. Melo, *J. Mater. Chem. A*, 2013, **1**, 1086–1095.

62 K. Panchal, K. Bhakar, K. S. Sharma, D. Kumar and S. Prasad, *Appl. Spectrosc. Rev.*, 2025, **60**, 30–55.

63 R. K. Mishra, G. J. Choi, Y. Sohn, S. H. Lee and J. S. Gwag, *Chem. Commun.*, 2020, **56**, 2893–2896.

64 G. Hariharan, S. Arunpandiyan, V. Shanmugapriya, S. Bharathi, M. Babu, B. Selvakumar and A. Arivarasan, *J. Energy Storage*, 2023, **57**, 106178.

65 D. Xu, W. Hu, X. N. Sun, P. Cui and X. Y. Chen, *J. Power Sources*, 2017, **341**, 448–456.

66 S. A. Sawant, M. R. Waikar, G. R. Chodankar, S. R. Gurav, A. V. Patil, R. S. Vhatkar and R. G. Sonkawade, *J. Energy Storage*, 2024, **76**, 109739.

67 N. Yadav, N. Yadav and S. Hashmi, *ACS Appl. Energy Mater.*, 2021, **4**, 6635–6649.

68 M. B. Idris, B. B. Mamba and F. Xolile, *RSC Adv.*, 2025, **15**, 48762–48774.

69 H. Choi, M.-C. Kim, Y. Park, S. Lee, W. Ahn, J. Hong, J. I. Sohn, A.-R. Jang and Y.-W. Lee, *J. Colloid Interface Sci.*, 2021, **588**, 62–69.

70 O. B. de Oliveira Moreira, L. V. de Faria, R. C. Matos, K. B. Enes, M. R. C. Couri and M. A. L. de Oliveira, *Anal. Methods*, 2022, **14**, 4784–4794.

71 W. Wang, V. Balland, M. Branca and B. Limoges, *J. Am. Chem. Soc.*, 2024, **146**, 15230–15250.